Geochimica et Cosmochimica Acta
September 2021, Volume 309, Pages 1-15
https://doi.org/10.1016/j.gca.2021.06.014
https://archimer.ifremer.fr/doc/00700/81167/

Mercury accumulation in the sediment of the Western Mediterranean abyssal plain: A reliable archive of the late Holocene

Cossa Daniel [1, 2, *], Mucci A [3], Guédron S. [1], Coquery M [4], Radakovich O. [5, 6], Escoube R. [2, 7], Campillo S. [1], Heussner S. [8]

[1] Université Grenoble Alpes, ISTerre, CS 40700, F-38058 Grenoble Cedex 9, France
[2] IFREMER, Atlantic Center, LBCM, F-44031 Nantes, France
[3] Geotop and Department of Earth and Planetary Sciences, McGill University, 3450 University St., Montreal, QC, H3A 0E8 Canada
[4] INRAE, UR RiverLy, 5 rue de la Doua CS 20244, F-69625 Villeurbanne, France
[5] IRSN (Institut de Radioprotection et de Sûreté Nucléaire), PSE-ENV/SRTE/LRTA, F-13115 Saint-Paul-lès-Durance, France
[6] Aix Marseille Université, CNRS, IRD, INRAE, Coll France, CEREGE, F-13545 Aix-en-Provence, France
[7] Université de Lyon, ESN Lyon, Earth Sciences Department, BP 7000, F-69342 Lyon Cedex 07, France
[8] Univeristé de Perpignan Via Domitia, CEFREM, UMR 5110, F-66860 Perpignan Cedex, France

* Corresponding author : Daniel Cossa, email address : dcossa@ifremer.fr

Abstract :

Temporal reconstruction of Hg deposition from sediment archives is relatively straightforward in organic-rich or high sedimentation rate environments, such as lakes and ocean margins. To retrieve long-term records at regional or global scales, deep-sea sediments are more appropriate, but such records are scarce and their reliability has been questioned because of possible post-depositional Hg diagenetic remobilization. Here, we investigated the accumulation of Hg in the Balearic Abyssal Plain (2850 m deep) of the Western Mediterranean through a comprehensive characterization of the chemical and isotopic composition (organic carbon, nitrogen, sulfur, major and redox-sensitive elements) of sediment trap material and sediment cores. The analysis of material collected in the sediment traps, deployed at 250, 1440, and 2820 m, indicates that Hg is (i) partially re-emitted to the atmosphere and mobilized in the twilight zone and that (ii) the Hg downward flux depends on the primary production in surface waters, suggesting that organic matter (OM) acts as the main Hg-carrier phase. As the Hg concentrations of material collected in the traps vary little with depth but the Hg:Corg ratio of the settling particulate matter decreases with depth, Hg must be re-adsorbed onto the more refractory fraction of the settling OM. Results of selective chemical extractions of the sediment indicate that Hg is very weakly coupled to the iron cycle but strongly associated with sulfur, supporting the assumption that its vertical distribution was only weakly altered by diagenetic remobilization. In addition, the distributions of S and δ34S in the sedimentary column exclude the possibility that local volcanism impacted on Hg enrichment of the sediments. Accordingly, a reconstruction of Hg accumulation rates (Hg-AR) during the Late Holocene is readily achieved. Biological mixing and smoothing of the sediment record, as revealed by the distribution

of radionuclides in surface sediments, was considered in the interpretation of the Hg-AR record. The first anthropogenic Hg signal recorded in the studied cores corresponds to the Iron Age and the Roman Empire period, as Hg-ARs rose from the baseline (0.7 ± 0.2 µg m-2 yr-1) to an average value of 2.2 ± 0.5 µg m-2 yr-1. The Hg-ARs return to baseline values at the decline of the Roman Empire, display a small increase during the Medieval Period (1.5 ± 0.5 µg m-2 yr-1), increase abruptly at the onset of the Industrial Era, leading to a ∼10-fold increase in Hg deposition in the last 120 years (8.9 ± 1.4 µg m-2 yr-1), and retreat progressively over the past 50 years.

Keywords : Mercury, Abyssal sediment, Holocene, Western Mediterranean

1. INTRODUCTION

Aquatic sediments can provide a record of trace element deposition from atmospheric and riverine sources, including evidence of natural and anthropogenic forcing (Bertine and Goldberg, 1977; Callender, 2003; Tribovillard et al., 2006). Historical reconstructions of trace element deposition from sediment archives are relatively straightforward if the element is not subject to strong diagenetic remobilization, of which Hg is a good example at least in organic-rich or high sedimentation rate environments such as lakes and marine coastal zones (Edgington and Robbins, 1976; Smith and Loring, 1981; Fitzgerald et al., 2018; Guédron et al., 2016). Natural sources of Hg to sediments are mainly from atmospheric and submarine volcanism, wildfires, and low-temperature volatilization from soils and some continental rocks (Fitzgerald and Lamborg, 2005; Mason et al., 2012). Anthropogenic Hg sources include high-temperature processes (fossil fuel and biomass burning, municipal waste incineration, etc.), mining activities, deforestation/erosion, industrial processes, and past domestic uses (Outridge et al., 2018; UN-Environment, 2019). Variations of Hg accumulation rates (Hg-AR) from natural and anthropogenic sources have been reported in sediment cores. The volcanic origin of Hg in sediments of the Triassic-Jurassic Muller Canyon (Nevada, USA) (Thibodeau et al., 2016; Thibodeau and Bergquist, 2017) and Permian Buchanan Lake (Canada) (Sanei et al., 2012) was well illustrated, whereas seafloor hydrothermal activity was revealed by elevated Hg concentrations in Holocene sediments of the northwestern Pacific (Lim et al., 2017). The impact of climate on Hg deposition, in response to changes in precipitation or biological productivity, has been identified in lakes and marine sediments (Outridge et al., 2007; Grasby et al., 2013; Kita et al., 2013, 2016; Guédron et al., 2018). Sediment records of anthropogenic Hg deposition in freshwater lakes as well as near-shore and ocean margin environments are numerous and have been used to document increases in global or local sources

(Cossa et al., 2001; Muir et al., 2009; Hare et al., 2010; Mucci et al., 2015). Several studies underscore the rapid increase in Hg deposition starting at the beginning of the Industrial Era, i.e., after AD 1850 (Azoury et al., 2013; Fitzgerald et al., 2018; Cooke et al., 2020). Enhanced Hg-ARs, linked to pre-industrial human activities, have been documented in strata of a Mediterranean lagoon sediment core dated to before ~AD 1850 (Elbaz-Poulichet et al. 2011). These authors highlighted two periods of increasing Hg deposition: the Middle Age, probably due to deforestation and biomass burning, and the XVI-XVIIth Centuries, most likely associated with the increase in Hg mining activities resulting from the development of the Hg amalgamation process for the recovery of silver and gold. Evidence of (pre-)historical anthropogenic Hg emissions has also been identified in lake sediments (Thevenon et al., 2011; Guédron et al., 2016; Cooke et al., 2009; Corella et al., 2017), including those associated with mining and metal treatment during the Bronze and Iron Ages (Elbaz-Poulichet et al., 2020). These results bolster the adequacy of aquatic sediments as geochronological records of Hg deposition.

Deep-sea sediments are of particular interest in this context since, given their slow accumulation rates, they can potentially provide an entire record of Holocene deposition even in short cores. Episodic depositional events (e.g., mass-wasting) or/and changes in redox conditions in response to a gradual or sudden modification of the sedimentation regime may, however, modify the sedimentary records of multivalent elements (Thomson et al., 1998; Crusius and Thomson, 2003). Mercury remobilization was documented at the oxic/suboxic boundary in deep-sea sediments where oxidation of pre-existing sulfides occurred (Mercone et al., 1999). Furthermore, chemical gradients across or near the sediment-water interface (SWI) can trigger a post-depositional redistribution of trace elements. Mercury enrichment at, or slightly below, the sediment-water interface (SWI) as well as downcore-decreasing concentrations were observed in

Arctic deep-sea sediments (Gobeil et al., 1999). Whereas increased anthropogenic Hg deposition was considered, the authors underlined that these profiles resulted from early diagenetic rearrangements of Hg in response to its affinity for authigenic Fe-oxyhydroxides that accumulate in the oxic layer. The effect of diagenetic remobilization was promoted by active bioturbation and low sedimentation rates, sedimentary conditions that are common to abyssal environments. In pelagic sediments of the Sea of Japan, Hg distributions display peaks near the SWI as well as in buried, brown "oxidized" sediment layers, also suggesting redox-driven diagenetic Hg redistribution (Kota, 2004). Conversely, in the sediment of the trench system and adjacent abyssal plain off the Kuril Islands, Hg burial is governed by atmospheric deposition and biological productivity. A Hg profile at this site, recording the last 120 years of deposition, features a maximum Hg flux corresponding to the second part of the XXth Century (Aksentov and Sattarova, 2020). Irrespective, biological mixing (bioturbation and bioirrigation) can smooth the sediment records resulting from marked changes in Hg deposition rates. To sum up, records of Hg accumulation in deep-sea sediments have been shown to reflect the chronology of paleo and (pre-)historical Hg deposition, but post-depositional Hg redistribution cannot be ruled out.

High-resolution vertical profiles of Hg concentrations were determined in three ~30-cm sediment cores recovered from the Balearic Abyssal Plain (BAP), covering the Late Holocene Period, in the Western Mediterranean (Fig. 1). These data, combined with analyses of settling particulate material collected at various depths in the water column, allowed us to interpret the Hg sedimentary records in terms of post-depositional dynamic and depositional chronology. Results show that post-depositional remobilization of Hg is minor and that, despite significant biological mixing, the Hg accumulation rates record the impact of the Iron Age, the Roman Empire, and the onset of the Industrial Era.

2. MATERIAL AND METHODS

2.1. Sampling

Undisturbed sediment cores (24-33 cm long) were obtained from three stations (A, B, C), roughly 25 km apart from each other, in the BAP (also called Algero-Balearic or Algero-Provencal Basin) of the Western Mediterranean Basin during a cruise onboard the R/V Urania in March 2001 (Fig. 1, Table 1). Cores were collected using a Wuttke-type multicorer and treated on-board immediately after recovery. Each core was sliced at 0.5 cm intervals over the first 5 cm, at 1 cm intervals from 5 to 20 cm, and at 2 cm intervals from 20 cm to the bottom.

At station C, three sediment traps (Technicap®, 0.125 m^2 diameter) were deployed along a mooring line at 250, 1440, and 2820 m depth, allowing the collection of 14 samples from each trap between April 2001 and April 2002 (Heussner et al., 1990; Zúñiga et al., 2007a). The samples were frozen immediately upon recovery, then freeze-dried, homogenized, and sub-sampled for various subsequent chemical analyses. Detailed descriptions of the cores and trapped material are given in the project final report (ADIOS, 2004).

2.2. Chemical analyses

Total Hg analyses were performed using an automatic atomic absorption spectrophotometer (AAS; Altec®, model AMA-254), according to the protocol described by EPA (2007). Briefly, weighed aliquots of freeze-dried sediment were introduced into the analytical system where they were heated to 550°C. The volatilized Hg was carried by a stream of oxygen to a gold trap onto which Hg was concentrated by amalgamation, before being thermally dissociated and analyzed by atomic absorption spectrometry. The detection limit was 7 ng g^{-1}, calculated as 3.3 times the standard deviation of the blanks. We used a marine sediment certified reference material (CRM)

(MESS-2 from the National Research Council of Canada) to ensure the accuracy of the analyses; the mean value obtained (92 ± 2 ng g^{-1}) was always within the range of the certified value: 92 ± 9 ng g^{-1}. The reproducibility, defined as the coefficient of variation of six replicate analyses of the same CRM was 1.8 %. The analytical uncertainty (EURACHEM/CITAC, 2000) is ~10 %. Labile Fe (and associated Hg) concentrations were estimated upon partial dissolution of the sediment with buffered ascorbate (pH 8.0) and dilute HCl (0.5 M) solutions according to protocols described by Kostka and Luther (1994). The ascorbate extraction is believed to dissolve only amorphous oxides, whereas the HCl extraction dissolves carbonates, crystalline Fe-oxyhydroxides, and acid volatile sulfides (AVS). It should be noted that the 0.5 M HCl extraction does not dissolve HgS (Mikac et al., 2000). To avoid losing the Hg^0 formed during the ascorbate extraction, the sample was not stirred continuously during the 24 h extraction, as the original protocol prescribes, but gently mixed a few times, and the resulting solution was analyzed immediately after the extraction and centrifugation.

The activities of ^{210}Pb in these cores were measured by alpha spectrometry of its daughter product ^{210}Po (see details in Angelidis et al., 2011). An additional set of ^{210}Pb activities were also obtained to refine the age-depth model between 13 and 20 cm in core B. They were acquired indirectly from the freeze-dried sediments by measuring the decay rate of its daughter isotope ^{210}Po by alpha spectrometry at the GEOTOP-UQAM Geochronology Laboratory. Uncertainties were estimated as two standard deviations (2s) for counting statistics, which is 4-8 % of the value obtained. A detailed description of the method can be found in Genovesi et al. (2011).

The total sulfur (S) and sulfur isotopic ratio (^{34}S:^{32}S) of the solids were measured on an Isoprime model VisIon isotope ratio mass spectrometer coupled to an Elementar Vario PyroCube elemental analyzer running in continuous flow mode at the Geotop-UQAM Light Stable Isotope Geochemistry Laboratory. The freeze-dried and crushed sediment samples were weighted in tin

cups to obtain similar amounts of SO_2 for all samples and reference materials. The elemental analyzer was calibrated against known amounts of sulfanilamide. Two internal reference materials (IAEA-S2 & IAEA-S3; $\delta^{34}S$ = +22.62 ± 0.16 ‰, and $\delta^{34}S$ = - 32.49 ± 0.16 ‰, respectively) were used to normalize the isotope ratios to the Vienna-Canyon Diablo Troilite *(VCDT)*. A third reference material (IAEA-S1; $\delta^{34}S$=-0.3 ± 0.00 ‰) was analyzed as an unknown to assess the exactness of the normalization. Results are reported in delta units (δ) in ‰ *vs* VCDT. The overall analytical uncertainty (2s), based on the propagation of uncertainties of the normalization of the internal reference materials and the samples, is better than ± 0.2 ‰, but it does not account for the homogeneity nor the representativity of the sample. Total sulfur concentrations and $\delta^{34}S$ values were corrected for the porewater sulfate contributions, using porosity values (Suppl. Info., Table S1) and assuming [SO_4^{2-}] was 0.0282 mole kg^{-1} and a 21 ‰ VCDT value for the modern ocean $\delta^{34}S$-SO_4^{2-} (Rees et al., 1978).

Major elements were analyzed by X-ray fluorescence spectrometry and results were published earlier (Angelidis et al., 2011). Total organic carbon (C_{org}) content and its isotopic composition ($\delta^{13}C_{org}$) were measured, after decarbonatation (Suppl. Info., SI.2), by Cavity Ring-Down Spectrometry (Picarro Inc.®) coupled to a Combustion Module (Costech Inc.®) (CM-CRDS) using previously reported analytical methods, calibration and sample preparation (Guédron et al., 2019 and references therein).

2.3. Age model and Hg accumulation rate calculation

The Hg-ARs within the 3 cores were obtained after computation of an age-depth model based on the ^{210}Pb activity data and the four radiocarbon ages reported in core C by Zúñiga et al. (2007b). The age-depth model was derived using the IntCal20 calibration curve (Reimer et al., 2020) with consideration of the marine reservoir [R(t) = 390 ± 85 y BP] age of the Mediterranean Sea (Siani

et al., 2000). Details of the derivation of the age-depth model can be found in Suppl. Info. (SI.3). Hg-ARs were computed with consideration of the sediment compaction following the equation:

$$\text{Hg-ARs} = 10*[\text{THg}]*\text{SR}*(1-\varphi)*d \quad (1)$$

where [THg] is the Hg concentration (ng g^{-1}, Fig. 5a), SR the sedimentation rate (cm yr^{-1}, Suppl. Info., SI.3), φ the porosity of the sediment (Suppl. Info., Table S1), and d the average grain sediment density, 2.65 g cm^{-3} according to Hamilton et al. (1976).

3. RESULTS

3.1. Sediment traps

The Hg and C_{org} concentrations of the particulate material collected by the sediment traps at Station C are reported in Table 2. Year-long Hg records displayed similar seasonal variations, irrespective of the trap/sampling depth, with the highest concentrations in spring and autumn, and the lowest in summer (Fig. 2). Interesting to note are the relatively high Hg concentrations during the Saharan dust events identified in July and November 2001 (ADIOS, 2004). Most striking are the nearly constant, mean particulate Hg concentrations throughout the water column (averaging 128 ± 23 ng g^{-1}, n = 42) whereas mean C_{org} concentrations decreased by a factor of ~3 between 250 and 2820 m depth (Table 2). In other words, the Hg concentrations in settling particles remain the same during their transit through the water column while particulate organic carbon is remineralized or dissolved. Accordingly, the Hg:C_{org} molar ratios increased from 0.06 to 0.15 x 10^{-6} between 250 and 2820 m.

3.2. Sediment cores

3.2.1. Sedimentary facies and geological settings

Several cores sampled at stations A, B, and C in the BAP during the same cruise (ADIOS, 2004) were described in two previous publications: one includes a description of their sequence stratigraphy and sediment lithology (Zúñiga et al., 2007b), whereas the other focusses on their trace element (Cu, Cd, Pb, Zn) composition (Angelidis et al., 2011). All the cores cover the Late Holocene Period and consist mainly of yellowish-brown, calcareous pelitic muds. They comprise five units (Fig. 3) referred to as U1 to U5 from the bottom to the top: two foraminifer–pteropod oozes (U1 and U4), two pteropod ooze layers (U2 and U5), and a turbidite deposit (U3). According to Zúñiga et al. (2007b), U3 is a zeolite-rich turbidite that likely originated from pyroclastic deposits derived from the Sardinian continental margin. For the three cores investigated in this study, U1 extended from the bottom of the cores to 14-16 cm below the sediment surface, whereas U5 occupied the top centimeter. The position of the other units in the sedimentary column varied slightly depending on the core: U2 was a 1-cm thick unit located between 13 and 16 cm from the surface, U3 was ~6-cm thick and found between 6 and 15 cm from the surface (7-13 cm, 9-15 cm, and 8-14 cm, for cores A, B, and C, respectively), and U4 was 6-8 cm thick and sat between 1 and 9 cm from the surface (Fig. 3).

3.2.2. Elemental distribution in the sedimentary column

At station B, the elemental composition of one core was determined to detail the chemo-stratigraphy of the sedimentary column (Fig. 4). Two notable features appear (i) high Ca/Fe values in U2 and U5, and (ii) a spike in Si/Al at the U2-U3 boundary (Fig. 4a, f). The first feature is coincident with a positive excursion of the $CaCO_3$ content (Suppl. Info., Fig. S3) which reflects the abundance of pteropods in units U2 and U5, whereas the Ca/Fe distinguishes turbidites from pelagites because of the higher Fe and lower Ca contents of turbidites in the BAP (Rothwell et al., 2006). On the other hand, high Si/Al and K/Al (Fig. 4f and Suppl. Info., Fig. S3) clearly indicate

the presence of a lithogenic layer that characterizes the turbiditic layer (U3) (Zúñiga et al., 2007b). Below the turbidite unit, several parameters abruptly increase, namely N_{tot} (and associated C_{org}/N_{tot} decrease), $\delta^{13}C_{org}$, S, and $\delta^{34}S$ (Fig. 4c, e, g, and h), whereas, HCl-extractible Fe and Mn decrease sharply (Fig. 4i and j). The C_{org}:N_{tot} molar ratios (<8) and $\delta^{13}C_{org}$ (>-25‰) indicate that the sedimentary organic carbon is mostly of marine (algal) origin (Meyers, 1994; Mackie et al., 2007). The $\delta^{34}S$ values in units U1, U2, U4, and U5 are close to the modern seawater value (~21 ‰), with lower values (<10 ‰) in unit U3 (Fig. 4g). The sharp, positive gradient of Fe_{HCl} and Mn_{HCl} concentrations at the interface of the U2-U3 units suggests that some Fe and Mn remobilization has occurred at this level despite the current oxic or suboxic redox conditions throughout the core (E_h > 180 mV, ADIOS, 2004). This gradient most likely developed (temporary suboxic or anoxic conditions in response to the respiration of fresh OM at the SWI) in response to the turbidite (U3) depositional event, which buried the former SWI, as previously suggested by Zúñiga et al. (2007b). The S and $\delta^{34}S$ sediment profiles (Fig. 4g and h) exhibit a slight decrease within the turbidite unit, a distinctive characteristic of the hosting zeolite mineral, an alteration product of volcanic material (Zúñiga et al., 2007b). A magmatic origin argues for low $\delta^{34}S$ values (Liotta et al., 2012).

3.2.3. Mercury distribution in the sedimentary column

Mercury profiles in the three sediment cores are shown in figure 5a. The Hg concentrations varied from 9 to 100 ng g^{-1}, with the highest values observed within the first 2 cm of the SWI and the lowest values at the bottom of the cores. The three Hg profiles exhibited the same vertical distribution patterns, characterized by an exponential decrease of Hg concentrations from the surface to the bottom of the cores, interrupted by a broad bump between 12 and 22 cm. These bumps reach 64, 89, and 58 ng g^{-1} in cores A, B, and C, respectively. Mercury concentrations covary with C_{org} ($R^2 = 0.52$, n = 81, $p<0.01$). Notwithstanding the bumps (between 12-22 cm) over

which the Hg:C_{org} molar ratios reach their highest value, the ratios decrease from ~1 x 10^{-6} at the sediment surface down to 0.17 x 10^{-6} at the bottom (Fig. 5c).

Vertical profiles of Hg-AR exhibited similar patterns for the 3 cores, with the lowest average Hg-AR values (0.7 ± 0.2 $\mu g \cdot m^{-2} \cdot yr^{-1}$) in the basal unit (depth > 23 cm in U1) (Fig. 5d). The Hg-AR background in marine sediments is poorly documented (see review by Cooke et al., 2020), but our minimum value is of the same order of magnitude as the background Hg-AR (ca. 1-2 $\mu g \cdot m^{-2} \cdot yr^{-1}$) recorded in various sediment archives (Lamborg et al., 2002; Serrano et al., 2013; de Simone et al., 2016; Cooke et al., 2020). Above 23 cm in U1, Hg-ARs increase up to 3.20, 3.95, and 2.47 $\mu g \cdot m^{-2} \cdot yr^{-1}$ in core A, B, and C respectively, followed by a rapid decline in U4 above the turbidite (averaging 1.0 ± 0.2 $\mu g \cdot m^{-2} \cdot yr^{-1}$ for the 3 cores). In U4, a low-amplitude "shoulder" is also visible between 3.5 and 6 cm in cores A and C (Fig. 5c, insert). Finally, the highest Hg-ARs (8.9 ± 1.4 $\mu g \cdot m^{-2} \cdot yr^{-1}$) are observed in the surface unit (U5), which includes the last ~120 years of deposition and is affected by mixing processes (Angelidis et al., 2011).

4. DISCUSSION

4.1. Mercury transfer from the atmosphere to the sediment

Despite the semi-enclosed nature of the Mediterranean Sea, the main Hg input to the open surface waters is, by far, from atmospheric deposition (e.g., Žagar et al., 2014). Little is known about the contributions of continental and hydrothermal inputs, except that mass-wasting events may reach the BAP (e.g., Cattaneo et al., 2020) and that hydrothermal fluxes, mostly located in the Tyrrhenian Sea, are rapidly transferred to the atmosphere (Bagnato et al., 2017). According to the data presented in Table 2, only 35 % of the atmospheric deposition flux (~34 ng m^{-2} d^{-1} according

to Gencarelli et al., 2014) is found in large particles collected in the 250-m deep sediment trap. Hence, these observations suggest that a significant (~65 %) amount of the Hg is re-emitted to the atmosphere, in agreement with results of global air-sea exchange oceanic budgets and models (e.g., Mason et al., 2012).

The Hg flux associated with settling particles collected at 250 m varied from 1.9 to 24.0 ng m^{-2} d^{-1} over the deployment period (Fig. 2); the range of this one-year-long record range is predictably broader than the range of Hg fluxes recorded in the Central Pacific during 24-hour sediment trap deployments (3.6 to 8.4 ng m^{-2} d^{-1} according to Munson et al., 2015). In the settling particles collected at 250 m during the sediment trap deployment above the BAP, the biogenic fraction was dominant (averaging 57 %). The concomitant, temporal variations of Hg concentrations and biogenic contents of the material collected in this trap (Fig. 2) as well as the positive correlation (R^2 = 0.60, $p<0.01$) between Hg concentrations and the monthly average Chlorophyll-a concentrations in surface waters (data from Zúñiga et al., 2007a) support the hypothesis that the vertical transfer of Hg through the water column is governed by phytoplanktonic uptake in the euphotic zone and the subsequent formation and settling of large biogenic particles in response to zooplankton grazing and excretion. However, irrespective of depth, there is no significant correlation between Hg and C_{org} concentrations in the trapped material. Biogenic material present in the settling particles of the Western Mediterranean consists of OM, calcium carbonates, and opal (Zúñiga et al 2007a), each component having a distinct affinity for Hg. In addition, the downward Hg flux is modulated by the lithogenic contribution (8-67 % according to Zúñiga et al., 2007a) to settling particles in the Mediterranean, ballasting biogenic material, especially during Saharan dust storms (Ternon et al., 2010). It is not surprising, owing to the diversity of settling particle composition, that its association with Hg is not directly accounted for

by the C_{org} proxy. Binding sites on OM are numerous and the stability of Hg complexes increases from carboxylic to thiolic groups (Haitzer et al., 2003; Ravichandran, 2003; Skyllberg et al., 2006; Liang et al., 2019). Using synchrotron-based X-ray Absorption Near-Edge Structure (XANES) and Extended X-ray Absorption Fine Structure (EXAFS) spectroscopy, it was discovered that, in laboratory bacterial cell suspensions, all divalent Hg ions were complexed to cell-bound thiolic functional groups (Mishra et al., 2017; Song et al., 2020). Complexation of methylmercury to phytoplanktonic cells may occur through the same mechanism (Skrobonja et al., 2019). In the absence of thiol and sulfur concentration data in the sediment trap material, the assumption that Hg is strongly associated to organic planktonic material and their debris is likely sound. This does not mean that the Hg concentration of settling particles is not, occasionally, affected by Saharan dust inputs. Very high Hg concentrations (~2 $\mu g\ g^{-1}$) have been measured in small particles of African dust collected in the Azores Islands as a result of emissions from open-pit Hg mines or the mined rock formations in Algeria (USGS, 2001). However, these findings are not confirmed by recent measurements performed on Saharan dust collected during a survey in the Canary Islands, where they are <100 ng g^{-1} (Bailey, 2021). Additional results are needed to clarify this issue.

Mercury associated with particles collected in traps located at 1440 and 2820-m depth only accounts for ca. 70 % of the total flux at 250 m. This implies that ca. one-third of the Hg is remobilized from the settling material between 250 and 1440 m. This depth interval, the so-called "twilight zone", which hosts heterotrophic activity, is the locus of net microbiological Hg methylation, with methylmercury (MeHg) accounting for up to 37 % of the THg (Cossa et al., 2009). Since MeHg has more affinity for the dissolved phase than inorganic Hg, Hg methylation is likely a critical mobilization process in the twilight zone. Below 1440 m, the Hg flux is invariant. Accordingly, the Hg:C_{org} ratio nearly triples between 250 and 2820 m (Table 2). This increase

reflects the preferential removal of Hg from the surface ocean relative to C export, as observed in the Pacific Ocean water column (Munson et al., 2015), and implies that Hg released upon the remineralization of particulate OM during settling through the water column must re-adsorb onto the residual particulate matter. Culture experiments have shown that Zn released from degrading phytoplankton is rapidly scavenged back onto settling OM (John and Conway, 2014). Such a process is likely relevant for Hg since conditional stability constants for Hg complexed to dissolved and particulate OM are larger than those of Zn (e.g., Feyte et al., 2010). During the scavenging process, the nature of the particulate Hg-OM binding sites probably changes as C_{org} is degraded during settling through the BAP water column, favoring the preferential binding of Hg to stronger ligands, such as thiol groups (Feyte et al., 2012; Liang et al., 2019; Guédron et al., 2020). Owing to the oxic conditions of the sediments, it can be expected that biogeochemical processes, similar to those occurring in the water column, control the Hg behavior in the sedimentary column. Nonetheless, the contrasting residence times in the two environments must be considered: the settling time of particles through a 2850 m water column is on the order of weeks, whereas the accumulation of a 30 cm thick sediment column is counted in thousands of years.

4.2. Diagenetic remobilization of mercury in the sediment column

Three main differences in the Hg and C_{org} geochemical behaviors are observed between sediment and settling particles collected in the traps. First, except for units U1 and U2, a strong correlation is found between the two parameters in the three cores ($R^2 = 0.80$, $p<0.01$, Suppl. Info. Fig. S4). Second, the Hg:C_{org} ratio in the sediments decreases with depth, in contrast to the particles that settles through the water column. Finally, whereas both Hg and C_{org} exhibit their highest concentrations in the first cm below the SWI (Fig. 5a and b) and the C_{org} concentrations decrease with increasing depth in the sediment (Fig. 5b) as a result of active microbial remineralization, the

decreasing Hg:C_{org} ratio (Fig. 5c) reflects a faster decreasing rate of Hg deposition with depth. This interpretation rests on the hypothesis that diagenetic Hg remobilization is limited, and supports a rise in anthropogenic Hg deposition in surficial sediments.

It has been proposed that the vertical distribution of Hg in Arctic deep sediments may be modulated by diagenetic remobilization and shuttling with the Fe cycle (Gobeil et al., 1999). In order to explore this possibility, we analyzed the Hg associated with amorphous iron oxides or ascorbate-extractable Fe (Fe_{asc}) in the BAP sediments. The Fe_{asc} fraction accounts for 0.7 ± 0.4 % of the total Fe, whereas the associated Hg (Hg_{asc}) accounts for 0.9 ± 0.7 % of the total Hg (Suppl. Info., Table S2). In addition, Hg_{asc} and Fe_{asc} are not correlated, except weakly in the first 5 cm of the sediments (R^2 = 0.51, $p<0.10$). Thus, our results indicate that the Hg associated with the amorphous iron oxide fraction is very small, implying that the amount of Hg diagenetically recycled with Fe oxides in BAP sediments is very limited. This conclusion is consistent with results of *in situ* experiments at a lacustrine sediment-water interface and modeling that show Hg to be preferentially bound to functional groups of the OM rather than to the hydroxyl groups of Fe-oxy(hydro)oxide surfaces (Feyte et al., 2010). The occurrence of the turbidite layer (U3), which capped the underlying layers (U1 and U2), also brings complementary insights about the potential redistribution of Hg resulting from a transitory redox change in the sediment column. The $\delta^{34}S$ values below the turbidite fail to indicate the presence of significant sulfate reduction products (Fig. 4h). Nonetheless, the sharp drop in Fe_{HCl} and Mn_{HCl} concentrations (Fig. 4i and j) immediately below the turbidite (U3) could be evidence of transient suboxic or anoxic conditions that developed at the top of the pteropod ooze (U2), fueled by the rapid burial of fresh OM that had accumulated at the former SWI. Under these conditions, reactive Mn and Fe in these sediments would have been reductively dissolved and migrated from U1 to U3 where the Fe and Mn were oxidized and

reprecipitated as authigenic oxides by the oxygen advected with the porewaters of the turbidite (Fig. 4i and j). A similar process has been described in detail for cores collected in a coastal environment subjected to a mass-wasting event (Mucci et al., 2003). In the BAP, the reductive dissolution of iron oxides below the turbidite, which might have occurred after the U3 turbidite deposition, is not accompanied by a decrease in Hg concentration as Hg concentrations peak within U1 (Fig. 5a). In other words, despite the microbial decay of fresh OM and the transitory development of reducing conditions that lead to the reductive dissolution of Fe oxides, Hg remained mostly immobile or was rapidly re-adsorbed onto the solid sediment including OM, as in the water column, through binding to reduced sulfur compounds. Indeed, the strong affinity of Hg for reduced sulfur seems to modulate both (i) scavenging through the water column and (ii) sediment sequestration following diagenetic remobilization. This hypothesis is supported by the strong correlations between the distributions of Hg and sulfur in the sediment of Core B (Fig. 6). Most of the variability in Hg concentrations in the deepest part (>23 cm) of the core, and in the turbidite unit (U3) of the sediment, is explained by the sulfur content, as illustrated by their respective correlations (R^2 = 0.65 and 0.74, $p<0.10$ *and* $p<0.05$). In these two layers, the Hg/S varies only slightly, whereas, in U1 (<23 cm), U2, U4, and U5, the regression coefficient of the Hg-S relationship is much higher (Fig. 6). It is interesting to note that in the turbidite (U3), in which a volcanic contribution has been ascertained (see section 3), there is no Hg anomaly that could hint at a geogenic origin (Fig. 6, insert). In other words, the distribution of Hg:S ratios through the core fails to reveal possible Hg inputs of volcanic or hydrothermal sources. The higher Hg:S ratio, in U1 (<23 cm), U2, U4, and U5 units (Fig. 6) could reflect the accumulation of fine cinnabar particles emitted to the Mediterranean atmosphere from the Almaden mines (Spain) since the beginning of their operation around 430 BC (Moreno et al., 2005).

At this stage, we can conclude that the participation of Hg in the diagenetic Fe-cycle in these abyssal sediments is limited and that a possible influence of local volcanism on Hg enrichment of the sediments is ruled out. Thus, the vertical distribution of Hg in the BAP likely provides an exploitable chronological record of Hg deposition during the Late Holocene Period, although smoothing by biological mixing must still be taken into consideration in the interpretation of this record.

4.3. Chronology of Hg fluxes and deposition

4.3.1. Modern deposition

Computed Hg-ARs for the first 2 cm (based on radionuclide profiles), which represent the last 120 years, averaged 9.8 ± 0.9, 8.3 ± 1.0, and 8.5 ± 1.8 μg m^{-2} yr^{-1} in cores A, B, and C, respectively (Figs. 5d and 7). Although the ^{210}Pb profile shows a classical decrease with depth (Suppl. Info., Fig. S1), a previous study using artificial radionuclides (^{137}Cs and $^{239,240}Pu$; Garcia-Orellana et al., 2009) divulges that the Hg signal has been smoothed by biological mixing. Even though they may carry large uncertainties, estimated surficial (0-1 cm) Hg-ARs (8.6 ± 1.9 μg m^{-2} yr^{-1}) for the last 50 years in the three cores are consistent with those (8.4 μg m^{-2} yr^{-1}) measured over the same period in the Ligurian Sea (Heimbürger et al., 2012). Although not directly comparable due to possible diagenetic processes in the nepheloid layer, these values are also consistent with those derived from the analysis of the sediment trap material recovered at 2820 m (3.1 ± 0.5 μg m^{-2} yr^{-1}, Table 2), which integrates the Hg deposition between 2001 and 2002. These lower recent deposition rates concur with the reported ~ 30% decrease of Hg concentrations in the western Mediterranean deep waters between 1989 and 2012 (Cossa et al., 2020) as well as with the reduced Hg emissions from utilities over the past two decades, that led to lower global anthropogenic emissions and associated deposition to ecosystems (Zhang et al., 2016). Overall, the observed sediment-surface Hg-

enrichment is consistent with the increasing global anthropogenic Hg emissions since the beginning of the Industrial Era (i.e., ~AD 1850 according to Outridge et al., 2018). The corresponding Hg-ARs are at least one order of magnitude larger than for the pre-Anthropocene epoch (i.e., before 1000 BC) background value (0.7 ± 0.2 µg m^{-2} yr^{-1}) in the three cores.

4.3.2. Pre- and historical Hg deposition

The first rise in Hg-ARs recorded in the 3 cores recovered in the BAP appears during the Iron Age period (i.e., the upper part of U1, ~800 to 50 BC), as Hg-ARs increased from the baseline (0.7 ± 0.2 µg m^{-2} yr^{-1}) to an average value of 2.5 ± 0.7 µg m^{-2} yr^{-1} (t-test, $p<0.01$). Because atmospheric circulation in the Mediterranean Basin is dominated by westerly winds (Ait Brahim et al., 2019; Azuara et al., 2020), the most probable source of Hg is the Iberian Peninsula where intense mining activities have been reported since the late Holocene period (Kassianidou and Knapp, 2005; Martinez-Cortizas et al, 1999), accounting for about half of the registered global Hg production in Europe (Hylander and Meili, 2003). Metal mining was also very active in Sardinia (Terpstra, 2021). This peak in Hg-AR is synchronous with the first $^{206/207}$Pb isotope anomaly (down to ~1.192) reported by Angelidis et al. (2011, Fig. 7, Suppl. Info., Fig. S1), and is consistent with known lead, silver, and cinnabar refining, smelting, and mining activities in Iberia during the Iron Age and Roman Empire (Nriagu, 1983). These activities are also recorded in other Mediterranean coastal sediments (Elbaz-Poulichet et al., 2011; Serrano et al., 2013), in a Spanish mire (Mártinez-Cortizas et al., 1997; 1999), and remote alpine lake sediments (Elbaz-Poulichet et al., 2020; Thevenon et al., 2011). In contrast to signals recorded in other archives, the dome-shaped Hg-AR record in the BAP sediments during the Iron Age and Roman Empire (Fig. 7) likely results from smoothing by biomixing of the geologically high-frequency variation of the anthropogenic signal. At the decline of the Roman Empire, ca. AD 200, Hg-ARs return to baseline values, just before the turbidite is

deposited (U3) (~AD 300). The latter was laid down at the same period as the Mediterranean megaturbidite was triggered by the AD 365 Crete earthquake and tsunami (Polonia et al., 2013). From that time on to ~AD 1800, Hg-ARs increase slightly and gradually from, on average, 1.0 ± 0.2 to 1.5 ± 0.5 μg m^{-2} y^{-1} in the 3 cores. Surprisingly, no marked peak was found corresponding to the Medieval Period (i.e., AD 500 to 1500), although this period is known for the massive development of metallurgy throughout Europe, including the intense metallurgical activities during the Islamic Period in Spain (AD 711 to 1492), a period documented by sharp increases in both Hg and Pb-ARs in almost all European records (Fig. 7, references herein). We consider that given the magnitude of the source, the low sedimentation rate, and the resolution of the BAP record, biomixing may have smoothed the signal and obliterated these short-duration mining peaks.

5. SUMMARY AND CONCLUSIONS

Temporal reconstruction of Hg deposition from sediment archives is relatively straightforward in organic-rich or high sedimentation rate environments since its diagenetic remobilization is limited compared to the large excursions in Hg emissions and deposition over the past 2000 years. Hg accumulation occurs mostly in areas, i.e., freshwater lakes or near-shore marine zones, close to point sources. To retrieve historical records on regional or global scales, deep-sea sediments are more appropriate. In addition, due to their slow accumulation rates, deep-sea sediments can provide deposition patterns over long periods, at least covering the Holocene. Such records are scarce, and their reliability has been questioned because of possible diagenetic remobilization, physical and biological mixing as well as post-depositional Hg redistribution resulting from mass-wasting processes (e.g., debris flows, submarine landslides/slumps, and turbidity currents). The sediment record of Hg deposition in the BAP of the Western Mediterranean - where sedimentation rates are

low (< 5 cm yr^{-1}) - is disrupted by episodic submarine slumps, transient redox gradients, and volcanic events. Nevertheless, our Hg sediment profiles, combined with analyses of sediment trap material recovered at different depths in the water column, allowed us to interpret its geochemical behavior through the water and sedimentary columns. Our results suggest that Hg deposited onto the ocean surface is (i) partially re-emitted from the surface waters to the atmosphere, (ii) taken up by plankton and sequestered mainly through complexation to thiolic functional groups of the biogenic material, (iii) partially mobilized and methylated in the twilight zone, and (iv) exported to the seafloor by the settling particulate organic matter. The vertical distributions of Hg, C_{org}, and S, as well as Fe speciation in the sediment, allow us to conclude that (i) a very limited amount of Hg is sorbed to amorphous Fe oxyhydroxides and, thus, the record of Hg deposition was not significantly affected by diagenetic remobilization, and (ii) hydrothermal or volcanic sources did not alter the Hg distribution. Hence, it is reasonable to propose that, in the Western Mediterranean, Hg is scavenged out of the water column and buried in the sediment as thiolate complexes, which may be converted to *β*-HgS according to the thermodynamically favorable reaction proposed by Manceau et al. (2015) for oxic soils. The formation of HgSe may further stabilize particulate Hg under suboxic conditions, as reported in other Mediterranean abyssal sediments (Mercone et al., 1999). We conclude that in the low C_{org} and low sedimentation rate BAP environment, Hg sedimentary profiles in ~30 cm cores are exploitable as chronological records of Hg deposition during the Late Holocene Period. In brief, owing to negligible diagenetic Hg remobilization and despite significant smoothing of the temporal variations of the Hg-ARs, the abyssal sediments of the Western Mediterranean preserve the imprints of major natural and anthropogenic Hg deposition. The Hg-AR rose from background values of 0.7 ± 0.2 μg m^{-2} y^{-1} μg m^{-2} y^{-1} in sediments deposited more than 5000 years ago, to 8.9 ± 1.4 μg m^{-2} y^{-1} in sediments deposited over the last century. The geochronological records highlight the imprints of the Iron Age, the Roman Empire,

a gradual increase of Hg depositions during the Medieval Period as well as the large contribution of the Industrial Era.

As a semi-enclosed sea, the Mediterranean receives Hg onto its surface waters and transfers it at depth at a higher rate than in the Pacific Ocean (Munson et al., 2015 and section 4.1.) and, consequently, its deep-sea sediments are more likely to provide a record of anthropogenic inputs. In contrast, the deep surficial sediments of the Arctic Ocean, another semi-enclosed sea, fail to show clear evidence of anthropogenic Hg contamination (Gobeil et al., 1999), although both systems export Hg to the North Atlantic Ocean (Cossa et al., 2018a; 2018b). This discrepancy most likely results from the relative strength of local Hg sources, the enhanced efficiency of Hg ballasting by aggregation of the biogenic carrier phase with Saharan dust, as well as the absence of significant Hg diagenetic rearrangement on the deep-sea Holocene sediments of the Mediterranean.

REFERENCES

ADIOS (2004) *Atmospheric deposition and Impact of Pollutants, key elements, and nutrients on the open Mediterranean Sea*. Final Report, Section 6: detailed report related to overall project duration. 93p. European Communities. Contract number: EVK3-CT-2000-00035 Coordinator: S. Heussner (CNRS, France).

Ait Brahim Y., Wassenburg J. A., Sha L., Cruz F. W., Deininger M., Sifeddine A., Bouchaou L., Spötl C., Edwards R. L. and Cheng H. (2019) North Atlantic Ice-Rafting, Ocean and Atmospheric Circulation During the Holocene: Insights From Western Mediterranean Speleothems. *Geophys. Res. Lett.* **46**, 7614-7623.

Aksentov K. I. and Sattarova V. V. (2020) Mercury geochemistry of deep-sea sediment cores from the Kuril area, northwest Pacific. *Progr. Oceanogr*. **180**, 102235.

Angelidis M. O., Radakovitch O., Veron A., Aloupi M., Heussner S., Price B. (2011) Anthropogenic metal contamination and sapropel imprints in deep Mediterranean sediments. *Mar. Pollut. Bull*. **62**, 1041-1052.

Azoury, S., Tronczynski J., Chiffoleau J.-F., Cossa D., Nakhlé K., Schmidt S. and Khalaf G. (2013) Historical Records of Mercury, Lead, and Polycyclic Aromatic Hydrocarbons Depositions in a Dated Sediment Core from the Eastern Mediterranean. *Environ. Sci. Technol*. **47**, 7101−7109.

Azuara J., Sabatier P., Lebreton V., Jalali B., Sicre M. A., Dezileau L., Bassetti M.A., Frigola J. and Coumbourieu-Nebout N. (2020) Mid- to Late-Holocene Mediterranean climate variability: Contribution of multi-proxy and multi-sequence comparison using wavelet analysis in the northwestern Mediterranean basin. *Earth Sci. Rev.* **208**, 103232.

Bagnato E., Oliveri E., Covelli S., Petranich E., Barra M., Italiano F., Prello F. and Sprovieri M. (2017) Hydrochemical mercury distribution and air-sea exchange over the submarine hydrothermal vents off-shore Panarea Island (Aeolian arc, Tyrrhenian Sea). *Mar. Chem.* **194,** 63-78.

Bailey N. (2021) Saharan Dust as a Mercury Transport Vector. M.Sc. thesis, Department of Environment and Geography, University of Manitoba, Winnipeg, Canada.

Bertine K. K. and Goldberg E. D. (1977) History of Heavy Metal Pollution in Southern California Coastal Zone-Reprise. *Environ. Sci. Technol*. **11**, 297-299.

Callender E. (2003) *Heavy Metals in the Environment—Historical Trends*. Treatise on Geochemistry, Vol. 9.03, 67-105. Turekian K. K., Holland H. D. editors. Elsevier Sciences.

Cattaneo A., Badhani S., Caradonna C., Bellucci M., Leroux E., Babonneau N., Garziglia S., Poort J., Akhmanov G. G., Bayon G., Dennielou B., Jouet G., Migeon S., Rabineau M., Droz L. and Clare M. (2020) The Last Glacial Maximum Balearic Abyssal Plain Megabed revisited. *Geol. Soc. Lond. Sp. Publ.* **500**, 341-357.

Cooke C. A., Wolfe A. P. and Hobbs W. O. (2009) Lake-sediment geochemistry reveals 1400 years of evolving extractive metallurgy at Cerro de Pasco, Peruvian Andes. *Geology* **37**, 1019–1022.

Cooke C. A, Martínez-Cortizas A., Bindler R. and Gustin M. S. (2020) Environmental archives of atmospheric Hg deposition – A review. *Sci. Total Environ*. **709**, 134800.

Corella J. P., Valero-Garcés B. L., Wang F., Martínez-Cortizas A., Cuevas C. A. and Saiz-Lopez A. (2017) 700 years reconstruction of mercury and lead atmospheric deposition in the Pyrenees (NE Spain). *Atmos. Environ*. **155**, 970–1107.

Cossa D., Elbaz-Poulichet F. and Nieto J. M. (2001) Mercury in the Tinto-Odiel Estuarine System (Gulf of Cadiz, Spain): Sources and Dispersion. *Aquat. Geochem.* **7**,_1-12.

Cossa, D., Averty B. and Pirrone N. (2009) The origin of methylmercury in the open Mediterranean water column. *Limnol. Oceanogr.* **54,** 837–844.

Cossa D., Heimbürger L.-E., Sonke J. E., Planquette H., Lherminier P., García-Ibáñez M. I., Pérez F. F. and Sarthou G. (2018a) Sources, recycling and transfer of mercury in the Labrador Sea (Geotraces-Geovide cruise). *Mar. Chem.* **198**, 64-69.

Cossa, D., Heimbürger L.-E., Pérez F. F., García-Ibáñez M. I., Sonke J. E., Planquette H., Lherminier P., Boutorh J., Cheize M., Menzel Barraqueta J. L., Shelley R. and Sarthou G. (2018b) Mercury distribution and transport in the North Atlantic Ocean along the Geotraces-GA01 transect. *Biogeosciences* **15**,_2309-2323.

Cossa D., Knoery J., Boye M., Marusczak N., Thomas B., Courau P. and Sprovieri S. (2020) Oceanic mercury concentrations on both sides of the Strait of Gibraltar decreased between 1989 and 2012. *Anthropocene* **29**, 100230.

Crusius J. and Thomson J. (2003) Mobility of authigenic rhenium, silver, and selenium during postdepositional oxidation in marine sediments *Geochim. Cosmochim. Acta* **67**, 265-273.

Edgington D. N. and Robbins J. A. (1976) Records of Lead Deposition in Lake Michigan Sediments Since 1800. *Environ. Sci. Technol*. **10**, 266-274.

Elbaz-Poulichet, F., Dezileau L., Freydier R., Cossa D. and Sabatier P. (2011) A 3500-year record of Hg and Pb contamination in a Mediterranean sedimentary archive (the Pierre Blanche Lagoon, France). *Environ. Sci. Technol*. **45**, 8642-8647.

Elbaz-Poulichet F., Guédron S., Anne-Lise D., Freydier R., Perrot V., Rossi M., Piot C., Delpoux S. and Sabatier P. (2020) A 10,000-year record of trace metal and metalloid (Cu, Hg, Sb, Pb) deposition in a western Alpine lake (Lake Robert, France): Deciphering local and regional mining contamination. *Quat. Sci. Rev.* **228**, 106076.

EPA (2007) Method 7473: *Mercury in Solids and Solutions by Thermal Decomposition, Amalgamation, and Atomic Absorption Spectrophotometry* (17 pp). https://www.epa.gov/sites/production/files/2015-12/documents/7473.pdf

EURACHEM/CITAC (2000) Quantifying uncertainty in analytical measurement. Tech. Rep. Guide CG4, EU-RACHEM/CITEC, EURACHEM/CITAC Guide. Second edition.

Feyte S., Tessier A., Gobeil C. and Cossa D. (2010) *In situ* adsorption of mercury, methylmercury and other elements by iron oxyhydroxides and associated organic matter in lake sediments. *Appl. Geochem.* **25**, 984-995.

Feyte S., Gobeil C., Tessier A. and Cossa D. (2012) Mercury dynamics in lake sediments *Geochim. Cosmochim. Acta* **82**, 92-112.

Fitzgerald W. F. and Lamborg C. H. (2005) *Geochemistry of mercury in the environment*. In: Lollar, B.S. Editor, Environmental Geochemistry. Elsevier–Pergamon, Oxford, pp. 107–148.

Fitzgerald W. F., Engstrom D. R., Hammerschmidt C. R., Lamborg C. H., Balcom P. H., Lima-Braun A. L., Bothner M. H. and Reddy C. M. (2018) Global and Local Sources of Mercury Deposition in Coastal New England Reconstructed from a Multiproxy, High-Resolution, Estuarine Sediment Record. *Environ. Sci. Technol*. **52**, 7614−7620.

Garcia-Orellana J., Pates J. M., Masqué P., Bruach J. and Sanchez-Cabeza J. (2009) Distribution of artificial radionuclides in deep sediments of the Mediterranean Sea. *Sci. Total Environ.* **407**, 887-898.

Gencarelli C. N., De Simone F., Hedgecock I. M., Sprovieri F. and Pirrone N. (2014) Development and application of a regional-scale atmospheric mercury model based on WRF/Chem: a Mediterranean area investigation. *Environ. Sci. Pollut. Res. Int.* **21**, 4095-109.

Genovesi L., de Vernal A., Thibodeau B., Hillaire-Marcel C., Mucci A. and Gilbert D. (2011) Recent changes in bottom water oxygenation and temperature in the Gulf of St. Lawrence: micropaleontological and geochemical evidence. *Limnol. Oceanogr.* **56**, 1319-1329.

Gobeil C., Macdonald R. W. and Smith J. N. (1999) Mercury profiles in sediments of the Arctic Ocean basins. *Environ. Sci. Technol*. **33**, 4194-4198.

Grasby S. E., Sanei, H. and Beauchamp B. (2013) Mercury deposition through the Permo-triassic Crisis. *Chem. Geol*. **351**, 209-216.

Guédron S., Amouroux D., Sabatier P., Desplanque C., Develle A.-L., Barre J., Feng, C., Guiter F., Arnaud F., Reyss J.-L. and Charlet L. (2016) A hundred year record of industrial and urban development in French Alps combining Hg accumulation rates and isotope composition in sediment archives from Lake Luitel. *Chem. Geol*. **431**, 10–19.

Guédron S., Ledru M.-P., Escobar-Torrezd K., Devellee A. L. and Brisseta E. (2018) Enhanced mercury deposition by Amazonian orographic precipitation: Evidence from high-elevation Holocene records of the Lake Titicaca region (Bolivia). *Palaeogeogr. Palaeoclimatol. Palaeoeco.* **511**, 577-587.

Guédron S., Tolu J., Brisset E., Sabatier P., Perrot V., Bouchet S., Develle A. L., Bindler R., Cossa D. and Fritz S. C. (2019) Late Holocene volcanic and anthropogenic mercury deposition in the western Central Andes (Lake Chungará, Chile). *Sci. Tot. Environ.* **662,** 903-914.

Guédron S., Audry S., Acha D., Bouchet S., Point D., Condom T., Heredia C., Campillo S., Baya P. A., Groleau A., Amice E. and Amouroux D. (2020) Diagenetic production, accumulation and sediment-water exchanges of methylmercury in contrasted sediment facies of Lake Titicaca (Bolivia). *Sci. Total Environ.* **723**, 138088.

Haitzer M., Aiken G. R. and Ryan J. N. (2003) Binding of Mercury(II) to Aquatic Humic Substances: Influence of pH and Source of Humic Substances. *Environ. Sci. Technol*. **37**, 2436-2441.

Hamilton E. L. (1976) Variations of density and porosity with depth in deep-sea sediments. *J. Sediment. Res.* **46**, 280-300.

Hare, A. A., Stern G. A., Kuzyk Z. Z. A., Macdonald R. W., Johannessen S.L. and Wang F. (2010) Natural and Anthropogenic Mercury distribution in Marine Sediments from Hudson Bay, Canada. *Environ. Sci. Technol*. **44**, 5805-5811.

Heimbürger L. E., Cossa D., Thibodeau B., Khripounoff A., Mas V., Chiffoleau J.-F., Schmidt S. and Migon C. (2012) Natural and anthropogenic trace metals in sediments of the Ligurian Sea (Northwestern Mediterranean). *Chem. Geol*. **291**, 141-151.

Heussner S., Ratti C. and Carbonne J. (1990) The PPS3 sediment trap and trap sample processing techniques used during the ECOMARGE experiment. *Cont. Shelf Res.* **10**, 943-958.

Hylander L. D. and Meili M. (2003) 500 years of mercury production: global annual inventory by region until 2000 and associated emissions. *Sci. Tot. Environ*. **304**, 13-27.

John S. G. and Conway T. M. (2014) A role for scavenging in the marine biogeochemical cycling of zinc and cadmium isotopes. *Earth Planet. Sci. Lett.* **394**, 159-167.

Kassianidou V. and Knapp A. B. (2005) *Archeometallurgy in the Mediterranean: The Social Context of Mining, Technology, and Trade.* Chap. 9. pp. 215-251. In: The archaeology of Mediterranean prehistory. Blake E. and A.B. Knapp editors. Blackwell Studies in global archaeology, Blackwell Publish. 333 p. Oxford, UK. ISBN 0-631-23267-2.

Kita I., Kojima M., Hasegawa H. et al. (2013) Mercury content as a new indicator of ocean stratification and primary productivity in Quaternary sediments off Bahama Bank in the Caribbean Sea. *Quater. Res.* **80**, 606–613.

Kita I., Yamashita T., Hasegawa H., Sato T. and Kuwahara Y. (2016) Mercury content in Atlantic sediments as a new indicator of the enlargement and reduction of Northern Hemisphere ice sheets. *J. Quaternary Sci*. **31**, 167-177.

Kostka J. E. and Luther G. W. (1994) Partitioning and speciation of solid phase iron in saltmarsh sediments *Geochim. Cosmochim. Acta* **58**, 1701-1710.

Kota F. S. (2004) Mercury in chemical fractions of recent pelagic sediments of the Sea of Japan. *J. Environ. Monit.* **6**, 689-695.

Lamborg C. H., Fitzgerald W. F., Damman A. W. H., Benoit J. M., Balcom P. H. and Engstrom D. R. (2002) Modern and historic atmospheric mercury fluxes in both hemispheres: Global and regional mercury cycling implications. *Global Biogeochem. Cycles* **16**, 1104.

Liang X., Lu X., Zhao J., Liang L., Zeng E. Y. and Gu B. (2019) Stepwise Reduction Approach Reveals Mercury Competitive Binding and Exchange Reactions within Natural Organic Matter and Mixed Organic Ligands. *Environ. Sci. Technol*. **53**, 10685−10694.

Lim D., Kim J., Xu Z. K., Jeong K. and Jung, H. (2017) New evidence for Kuroshio inflow and deepwater circulation in the Okinawa Trough, East China Sea: Sedimentary mercury variations over the last 20kyr. *Paleoceanography* **32**, 571-579.

Liotta M., Rizzo A., Paonita A., Caracausi A. and Martelli M. (2012) Sulfur isotopic compositions of fumarolic and plume gases at Mount Etna (Italy) and inferences on their magmatic source, *Geochem. Geophys. Geosyst*., **13**, Q05015.

Mackie E. A. V., Lloyd J. M. and Leng M. J. (2007) Assessment of $\delta^{13}C$ and C/N ratios in bulk organic matter as palaeosalinityindicators in Holocene and Late glacial isolation basin sediments, northwest Scotland. *J. Quat. Sci*. **22**, 579–591.

Manceau A., Lemouchi C., Enescu M., Gaillot A. C., Lanson M., Magnin V., Glatzel P., Poulin B. A., Ryan J. N., Aiken G. R., Gautier-Luneau I. and Nagy K. L. (2015) Formation of Mercury Sulfide from Hg(II)−Thiolate Complexes in Natural Organic Matter. *Environ. Sci. Technol*. **49**, 9787-9796.

Martinez-Cortizas A., Pontevedra-Pombal X., Munoz J. N. and García-Rodeja E. (1997) Four thousand years of atmospheric Pb, Cd and Zn deposition recorded by the ombrotrophic peat bog of Penido Vello (Northwestern Spain). *Water Air Soil Pollut.* **100**, 387-403.

Martinez-Cortizas A., Pontevedra-Pombal X., Garcia-Rodeja E., Novoa-Munoz J. C. and Shotyk W. (1999) Mercury in a Spanish peat bog: archive of climate change and atmospheric metal deposition. *Science* **284**, 939-942.

Mason R. P., Choi A. L., Fitzgerald W. F., Hammerschmidt C. R., Lamborg C. H., Soerensen A. L. and Sunderland E. M. (2012) Mercury biogeochemical cycling in the ocean and policy implications. *Environ. Res*. **119**, 101-117.

Mercone D., Thomson J., Croudace I. W. and Troelstra S. R. (1999) A coupled natural immobilisation mechanism for mercury and selenium in deep-sea sediments *Geochim. Cosmochim. Acta* **63**, 1481-1488.

Meyers P. A. (1994) Preservation of elemental and isotopic source identification of sedimentary organic matter. *Chem. Geol.* **114**, 289–302.

Mikac N., Niessen S., Ouddane B. and Fisher J.-C. (2000) Effects of Acid Volatile Sulfides on the Use of Hydrochloric Acid for Determining Solid-Phase Associations of Mercury in Sediments. *Environ. Sci. Technol*. **34**, 1871-1876.

Mishra B., Shoenfelt E., Yu Q., Yee N., Fein J. B., Myneni S. C. B. (2017) Stoichiometry of mercury-thiol complexes on bacterial cell Envelopes. *Chem. Geol*. **464**, 137-146.

Moreno T., Higueras P., Jones T., McDonald I. and Gibbons W. (2005) Size fractionation in mercury-bearing airborne particles (HgPM10) at Almade´n, Spain: Implications for inhalation hazards around old mines. *Atmos. Environ*. **39**, 6409-6419.

Mucci A., Boudreau B. and Guignard C. (2003) Diagenetic mobility of trace elements in sediments covered by a flash flood deposit: Mn, Fe and As. *Appl. Geochem.* **18**, 1011-1026.

Mucci A., Bernier G. and Guignard C. (2015) Mercury remobilization in Saguenay Fjord (Quebec, Canada) sediments: Insights following a mass-flow event and capping efficiency. *Appl. Geochem*. **54**, 13-26.

Muir D. C. G., Wang X. Yang F., Nguyen N., Jackson T. A., Evans M. S., Douglas M., Köck, G., Lamoureux S., Pienitz R., Smol J. P., Vincent W. F. and Dastoor A. (2009) Spatial Trends and Historical Deposition of Mercury in Eastern and Northern Canada Inferred from Lake Sediment Cores. *Environ. Sci. Technol*. **43**, 4802-4809.

Munson K. M., Lamborg C. H., Swarr G. J. and Saito M. A. (2015) Mercury species concentrations and fluxes in the Central Tropical Pacific Ocean. *Global Biogeochem. Cycle* **29**, 656-676.

Nriagu J. O. (1983) Occupational exposure to lead in ancient times. *Sci. Total Environ*. **31**, 105-116.

Polonia A., Bonatti E., Camerlenghi A., Lucchi R. G., Panieri G. and Gasperini L. (2013) Mediterranean megaturbidite triggered by the AD 365 Crete earthquake and tsunami. *Sci. Rep.-UK* **3**, 1285.

Outridge P. M., Sanei H., Stern G. A., Hamilton P. B. and Goodarzi F. (2007) Evidence for control of mercury accumulation in sediments by variations of aquatic primary productivity in Canadian High Arctic lakes. *Environ. Sci. Technol*. **41**, 5259–5265.

Outridge P. M., Mason R. P., Wang F., Guerrero S. and Heimbürger-Boavida L. E. (2018) Updated Global and Oceanic Mercury Budgets for the United Nations Global Mercury Assessment 2018. *Environ. Sci. Technol.* **52**, 12968–12977.

Ravichandran M. (2003) Interactions between mercury and dissolved organic matter, A Review. *Chemosphere* **55**, 319-331.

Rees C. E., Jenkins W. J., Monster J. (1978) The sulphur isotopic composition of ocean water sulphate. *Geochim. Cosmochim. Acta* **42**, 377–381.

Reimer P. J., Austin W. E. N., Bard E., Bayliss A., Blackwell P. G., Bronk Ramsey C., Butzin M., Cheng H., Edwards R. L., Friedrich M., Grootes P. M., Guilderson T. P., Hajdas I., Heaton T. J., Hogg A. G., Hughen K. A., Kromer B., Manning S. W., Muscheler R., Palmer J. G., Pearson C., van der Plicht J., Reimer R. W., Richards D. A., Scott E. M., Southon J. R., Turney C. S. M., Wacker L., Adolphi F., Büntgen U., Capano M., Fahrni S. M., Fogtmann-Schulz A., Friedrich R., Köhler P., Kudsk S., Miyake F., Olsen J., Reinig F., Sakamoto M., Sookdeo A. and Talamo S. (2020) The IntCal20 Northern Hemisphere Radiocarbon Age Calibration Curve (0–55 cal kBP). *Radiocarbon* **62**, 725-757.

Rothwell R. G., Hoogakker B., Thomson J., Croudace I. W. and Frenz M. (2006) *Turbidite emplacement on the southern Balearic Abyssal Plain (western Mediterranean Sea) during Marine Isotope Stages 1-3: an application of ITRAX XRF scanning of sediment cores to lithostratigraphic analysis*. Geological Society, London, Special Publications **267**, 79-98.

Sanei H., Grasby S. E. and Beauchamp B. (2012) Latest Permian mercury anomalies. *Geology* **40**, 63–66.

Serrano O., Mártinez-Cortizas A., Mateo M. A., Biester, H. and Bindler R. (2013) Millennial scale impact on the marine biogeochemical cycle of mercury from early mining on the Iberian Peninsula. *Global Biogeochem. Cycles* **27**, 21-30.

Siani G., Paterne M., Arnold M., Bard E., Métivier B., Tisnerat N. and Bassinot F. (2000) Radiocarbon Reservoir Ages in the Mediterranean Sea and Black Sea. *Radiocarbon* **42**, 271-280.

de Simone F., Gencarelli C. N., Hedgecock I. M. and Pirrone N. (2016) A Modeling Comparison of Mercury Deposition from Current Anthropogenic Mercury Emission Inventories. *Environ. Sci. Technol*. **50**, 5154-5162.

Skrobonja A., Gojkovic Z., Soerensen A. L., Westlund P. O., Funk C. and Bjorn E. (2019) Uptake Kinetics of Methylmercury in a Freshwter Alga Exposed to Methylmercury Complexes with Environmentally Relevant Thiols. *Environ. Sci. Technol*. **53**, 13757-13766.

Skyllberg U., Bloom P. R., Qian J., Lin C.-M. and Bleam W. F. (2006) Complexation of Mercury(II) in Soil Organic Matter: EXAFS Evidence for Linear Two-Coordination with Reduced Sulfur Groups. *Environ. Sci. Technol.* **40**, 4174-4180.

Smith J. N. and Loring D. H. (1981) Geochronology for mercury pollution in the sediments of the Saguenay Fjord, Quebec. *Environ. Sci. Technol*. **15**, 944-951.

Song Y., Adediran G. A., Jiang T., Hayama S., Björn E. and Skyllberg U. (2020) Toward an Internally Consistent Model for Hg(II) Chemical Speciation Calculations in Bacterium−Natural Organic Matter−Low Molecular Mass Thiol Systems. *Environ. Sci. Technol*. **54**, 8094−8103.

Ternon E., Guieu C., Loÿe-Pilot M.-D., Leblond N., Bosc E., Gasser B., Miquel J.-C. and Martín J. (2010) The impact of Saharan dust on the particulate export in the water column of the North Western Mediterranean Sea. *Biogeosciences* **7**, 809–826.

Terpstra T. T. (2021) Mediterranean silver production and the site of Antas, Sardina. *Oxf. J. Archaeol.* **40**, 176-190.

Thevenon F., Guédron S., Chiaradia M., Loizeau J.-L. and Poté J. (2011) (Pre-) historic changes in natural and anthropogenic heavy metals deposition inferred from two contrasting Swiss Alpine lakes. *Quaternary Sci. Rev*. **30**, 224-233.

Thibodeau A. M., Ritterbush K., Yager J. A., West A. J., Ibarra Y., Bottjer D. J., Berelson W. M., Bergquist B. A. and Corsetti F. A. (2016) Mercury anomalies and the timing of biotic recovery following the end-Triassic mass extinction: *Nature Com*. **7**, 1–8.

Thibodeau A. M. and Bergquist B. A. (2017) Do mercury isotopes record the signature of massive volcanism in marine sedimentary records? *Geology* **45**, 95–96.

Thomson J., Jarvis I., Green D. R. H., Green, D. A. and Clayton T. (1998) Mobility and immobility of redox-sensitive elements in deep-sea turbidites during shallow burial. *Geochim. Cosmochim. Acta* **62**, 643–656.

Tribovillard N., Algeo T. J., Lyons T. and Riboulleau A. (2006) Trace metals as paleoredox and paleoproductivity proxies: an update. *Chem. Geol*. **232**, 12–32.

UN-Environment 2019. *Global Mercury Assessment 2018*. United Nation Environmental Programme, Chemicals and Health Branch, Programme Chemicals and Health Branch Geneva

Switzerland. ISBN 978-92-807-3744-8. https://www.unenvironment.org/resources/publication/global-mercury-assessment-2018.

USGS (2001) African Dust Causes Widespread Environmental Distress. *Open-File Report 01-246*, U.S. Geological Survey, July 2001.

Žagar D., Sirnik N., Četina M., Horvat M., Kotnik J., Ogrinc N., Hedgecock I. M., Cinnirella S., de Simone F., Gencarelli C. N. and Pirrone N. (2014) Mercury in the Mediterranean. Part 2: processes and mass balance. *Environ. Sci. Pollut. Res.* **21**, 4081–4094.

Zhang Y., Jacob D. J., Horowitz H. M., Chen L., Amos H. M., Krabbenhoft D. P., Slemr F., St. Louis V. L. and Sunderland E.M. (2016) Observed decrease in atmospheric mercury explained by global decline in anthropogenic emissions. *Proc. Natl. Acad. Sci. U.S.A.* **113**, 526-531.

Zúñiga D., Calafat A. Sanchez-Vidal A., Canals M., Price N. B., Heussner S. and Miserocchi S. (2007a) Particulate organic carbon budget in the open Algero-Balearic Basin (Western Mediterranean): Assessment from a one-year sediment trap experiment. *Deep-Sea Res. I* **54**, 1530-1548.

Zúñiga D., Garcia-Orellana J., Calafat A., Price N. B., Adatte T., Sanchez-Vidal A., Canals M., Sanchez-Cabeza J. A., Masque P. and Fabres J. (2007b) Late Holocene fine-grained sediments of the Balearic Abyssal Plain, Western Mediterranean Sea. *Mar. Geol*. **237**, 25–36.

Declaration of Competing Interest

The authors declare that they have no known competing financial interests or personal relationships that could have appeared to influence the work reported in this paper.

ACKNOWLEDGEMENTS

This work was supported financially by the European Community in the framework of the ADIOS MAST program (EVK3-CT-2000-00035, Atmospheric deposition and impact of pollutants on the open Mediterranean Sea). We would like to thank Jean-Francois Hélie and Bassam Ghaleb at GEOTOP-UQAM for carrying out the total sulfur, $\delta^{34}S$ and complementary ^{210}Pb analyses. These analyses were subsidized by a Regroupement Stratégique grant from the Fonds Québécois de Recherche Nature et Technologies (FQRNT) to GEOTOP as well as an NSERC Discovery

grant to A.M. We would also like to thank Pascale Occhipinti and Laurent Nectoux for the Hg analyses performed at the INERIS, and Roselyne Buscail for providing the C and N data. Thanks are due to Neal Bailey and Feiyue Wang (University of Manitoba, Center for Earth Observation Science, Winnipeg, Canada) for providing Hg concentration levels in the Saharan dust collected in the Canary Islands and Cape Verde. The comments of reviewers allowed to improve the manuscript, their anonymous authors are sincerely thanked.

TABLES

Table 1. *Location, water depths of the multicore stations, and sediment core lengths in the Balearic Abyssal Plain of the Western Mediterranean.*

Station (core)	Latitude N	Longitude E	Depth (m)	Core length (cm)
A	39°28.30’	5°57.37’	2850	22
B	39°29.51’	6°10.88’	2854	32
C	39°18.81’	6°04.22’	2854	30

Table 2. *Mercury concentrations (mean ± standard deviation) in material recovered from sediment traps deployed at site C (Fig. 1, Table 1) between April 2001 and April 2002. Particulate organic carbon (POC) data are from Zúñiga et al. (2007a). Water column depth above sediments: 2854 m. Average atmospheric Hg deposition onto Mediterranean Sea surface waters is ca. 34 ng m^{-2} d^{-1} (Gencarelli et al., 2014).*

Depth (m)	Hg (ng g^{-1})	C_{org} (%)	Hg/C_{org} (molar ratio 10^{-6})	POC flux (mg m^{-2} d^{-1})	Hg flux (ng m^{-2} d^{-1})
250	127 ± 30	13.4 ± 5.2	0.057	9.9	12.2 ± 8.2
1440	126 ± 19	6.7 ± 2.3	0.112	3.8	8.8 ± 5.5
2820	130 ± 20	5.1 ± 1.3	0.152	2.9	8.6 ± 6.2

FIGURE CAPTIONS

Figure 1. *Sampling location of sediment cores A, B, and C in the Balearic Abyssal Plain of the Western Mediterranean (see also Table 1).*

Figure 2. *Temporal variation of Hg concentrations in the material recovered from the sediment traps moored at station C between April 2001 and April 2002. Average biogenic content (organic matter, calcium carbonate, and opal) modified from figure 6 in Zúñiga et al. (2007a).*

Figure 3. *Information logs of sediment cores A, B, and C, showing geological units according to Zúñiga et al. (2007b): Pteropod ooze layers (U2 and U5), foraminifer–pteropod oozes (U1 and U4), and turbidite unit (U3) between 7-13 cm, 9-15 cm, and 8-14 cm, for cores A, B, and C, respectively. See text for details. Note that several multicorer samplings were performed at each site during the R/V Urania cruise in 2001. Hence, core B analyzed in this study is the same as the one described by Angelidis et al. (2011), but different from core B described by Zúñiga et al. (2007b).*

Figure 4*. Elemental composition of sediment core B.*

Figure 5. *Total mercury (Hg), Hg accumulation rate (Hg-AR), and Hg:C_{org} ratio profiles in sediment cores A, B, and C.*

Figure 6*. Mercury (Hg)* versus *sulfur (S) concentrations in core B. The Hg:S ratio profile in sediment core B is given in the insert.*

Figure 7*. Hg accumulation rates (Hg-AR) for marine, lacustrine, and mire sediment historical records. Records are presented according to their geographical location from west to east following the trade wind direction (westerlies) from bottom to top: Penido Vello mire (Spain, Mártinez-Cortizas et al., 1999), Portlligat Bay marine sediment (Spain, Serrano et al., 2013), cores A, B, and C marine sediment from the Balearic Abyssal plain (this study), and two headwater catchment lake records from the western (Robert, France, Elbaz-Poulichet et al., 2020) and central Alpes (Meidsee, Switzerland, Thevenon et al., 2011).*

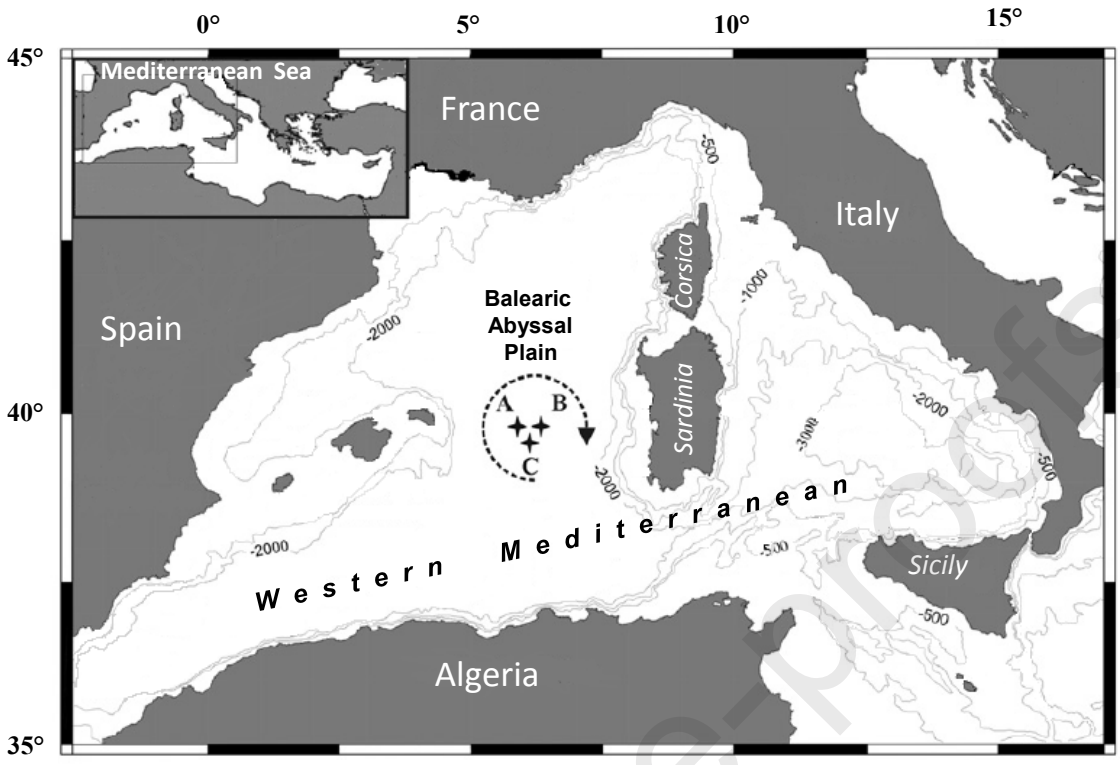

Fig. 1

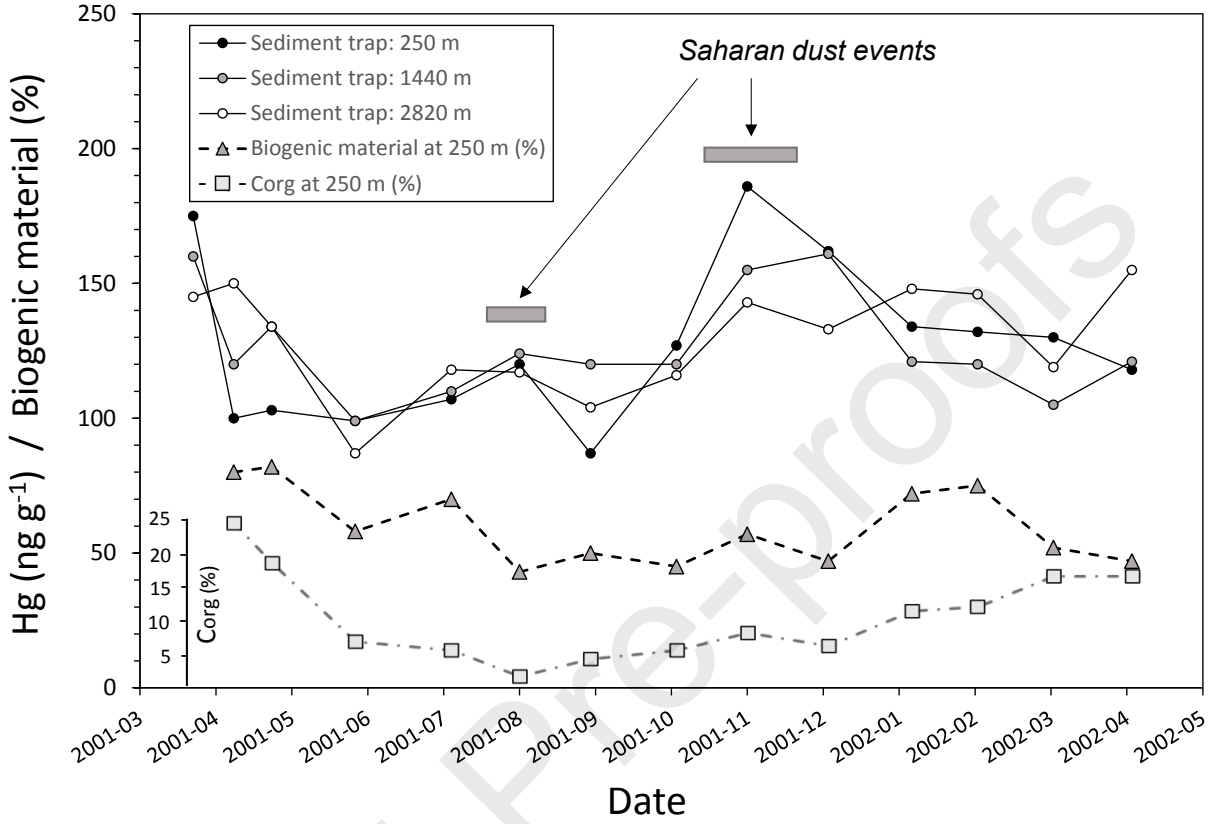
Sediment trap: 250 m
Sediment trap: 1440 m
Sediment trap: 2820 m
Biogenic material at 250 m (%)
Corg at 250 m (%)
Saharan dust events
Hg (ng g-1) / Biogenic material (%)
Corg (%)
Date
2001-03
2001-04
2001-05
2001-06
2001-07
2001-08
2001-09
2001-10
2001-11
2001-12
2002-01
2002-02
2002-03
2002-04
2002-05

Fig. 2

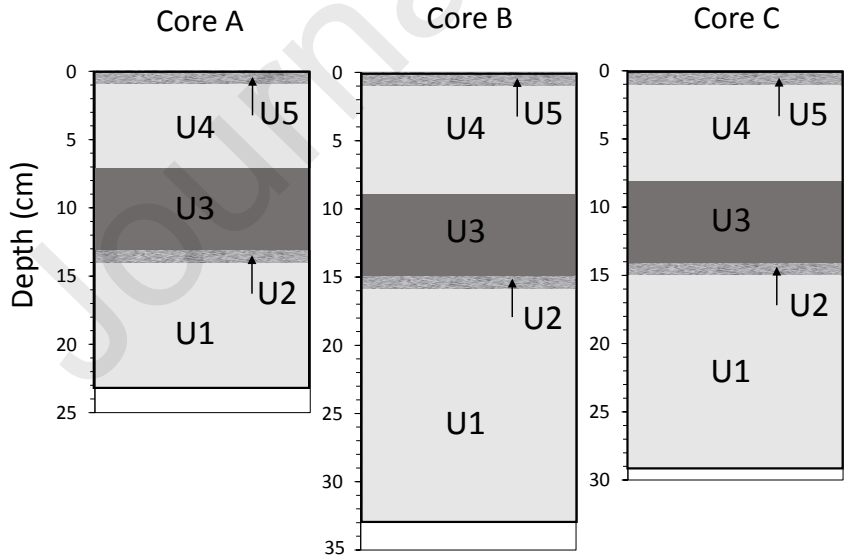
Core A
Core B
Core C
Depth (cm)
U1
U2
U3
U4
U5

Fig. 3

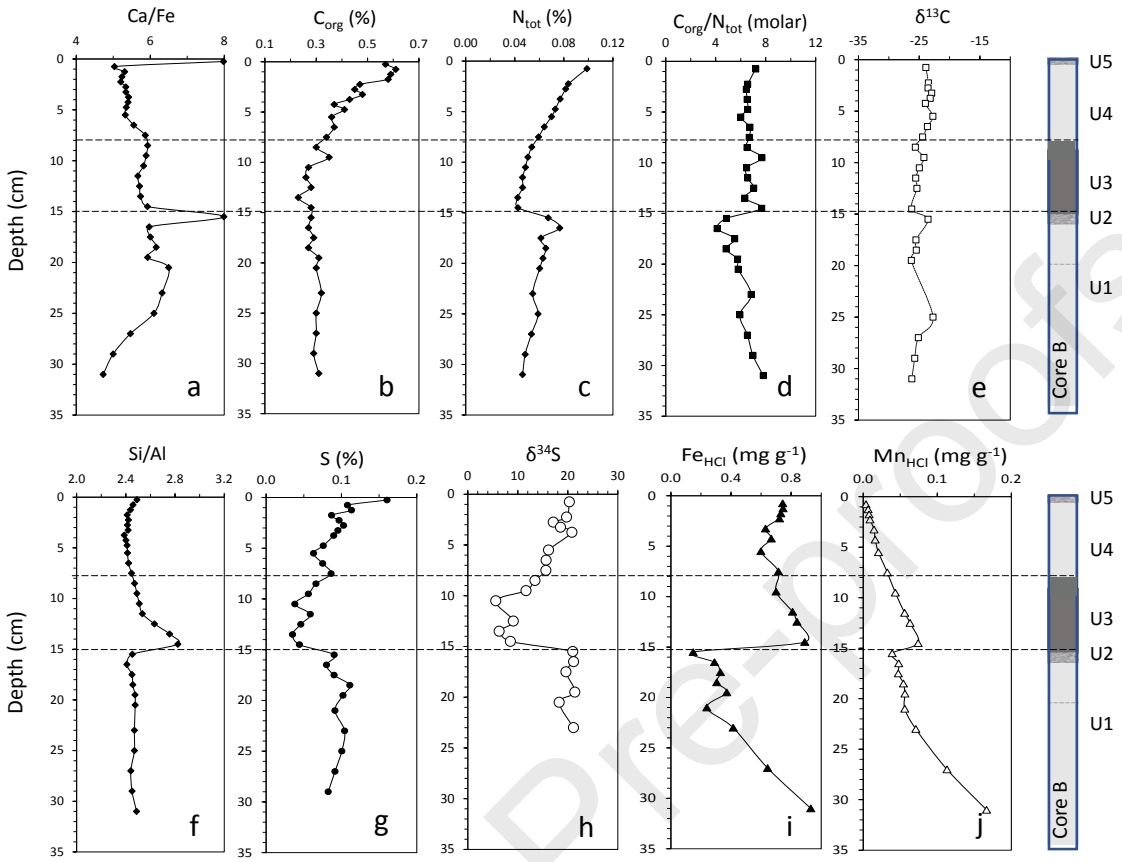
Ca/Fe
Corg (%)
Ntot (%)
Corg/Ntot (molar)
δ13C
Si/Al
S (%)
δ34S
FeHCl (mg g-1)
MnHCl (mg g-1)
Depth (cm)
U5
U4
U3
U2
U1
Core B
a
b
c
d
e
f
g
h
i
j

Fig. 4

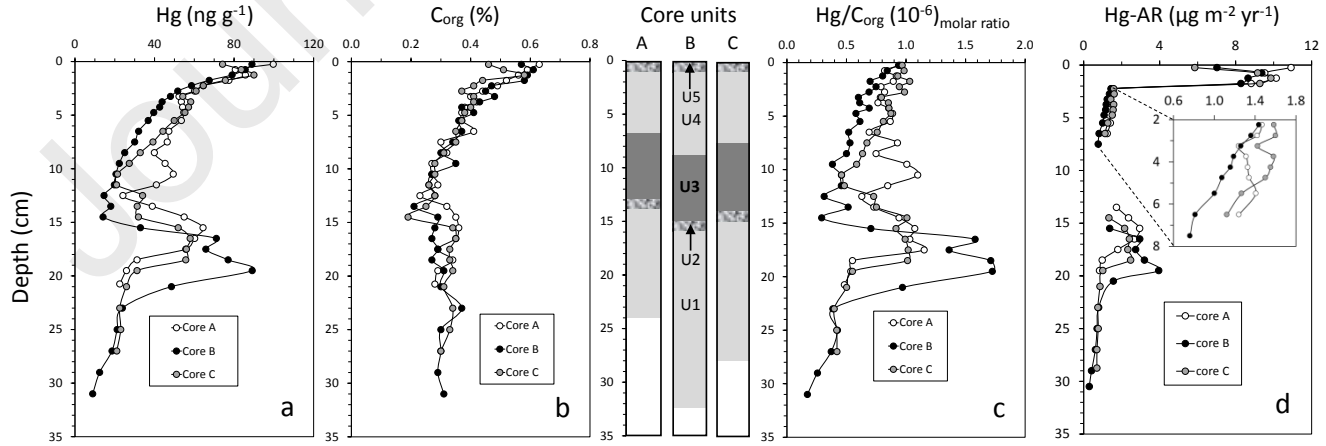
Hg (ng g-1)
Corg (%)
Core units
Hg/Corg (10-6)molar ratio
Hg-AR (µg m-2 yr-1)
Depth (cm)
A
B
C
U5
U4
U3
U2
U1
Core A
Core B
Core C
core A
core B
core C
a
b
c
d

Fig. 5

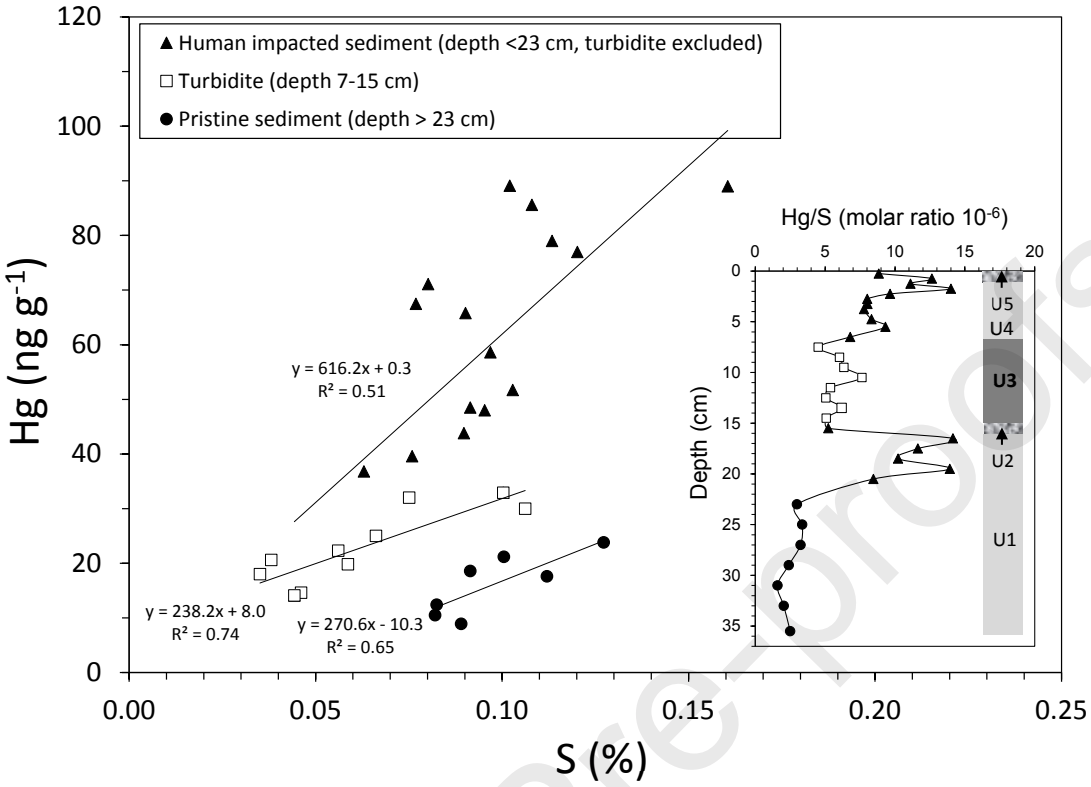

Fig. 6

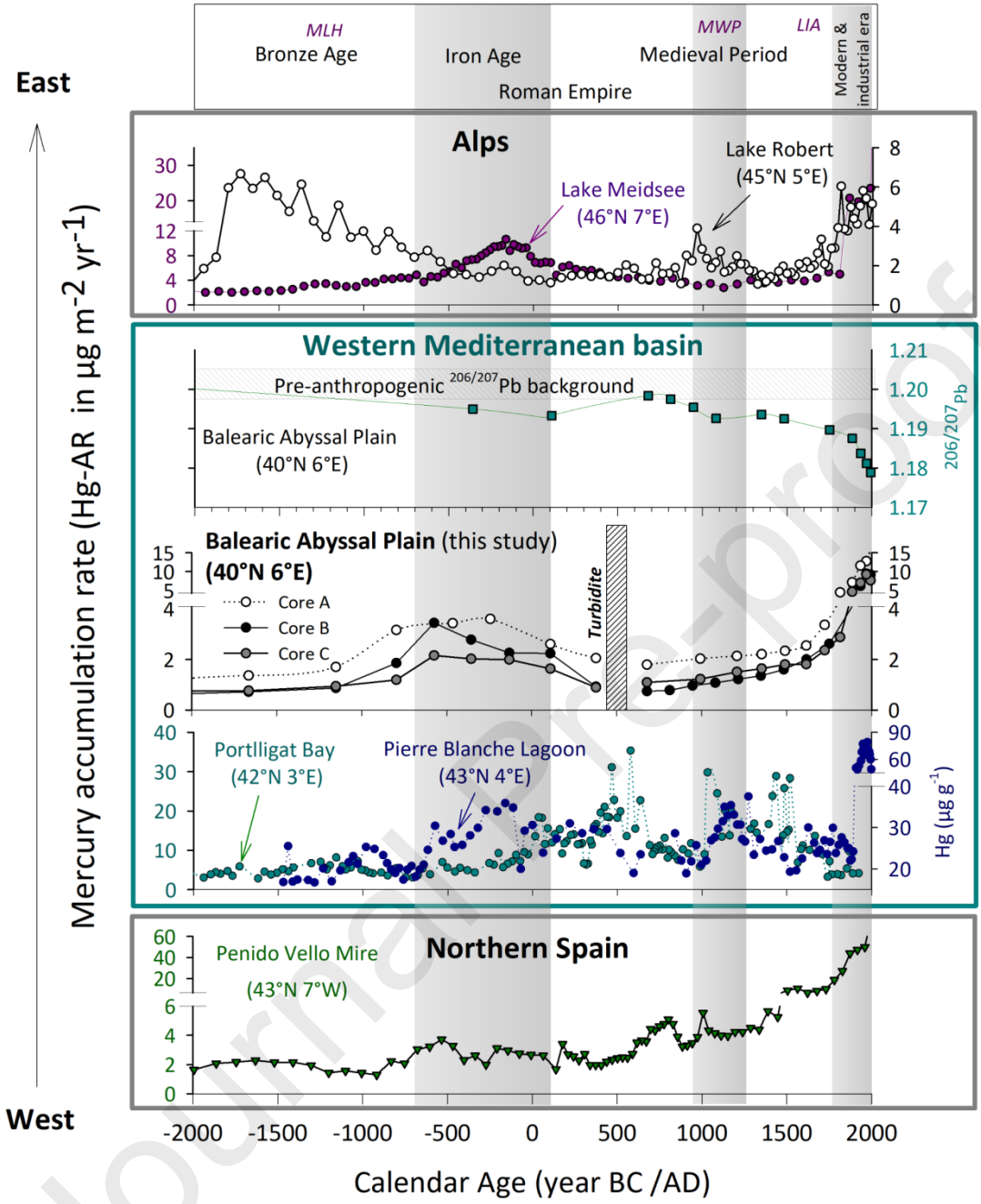
MLH
Bronze Age
Iron Age
Roman Empire
MWP
Medieval Period
LIA
Modern & industrial era
East
West
Alps
Lake Meidsee
(46°N 7°E)
Lake Robert
(45°N 5°E)
Western Mediterranean basin
Pre-anthropogenic 206/207Pb background
Balearic Abyssal Plain
(40°N 6°E)
206/207Pb
Balearic Abyssal Plain (this study)
(40°N 6°E)
Core A
Core B
Core C
Turbidite
Portlligat Bay
(42°N 3°E)
Pierre Blanche Lagoon
(43°N 4°E)
Hg (µg g-1)
Northern Spain
Penido Vello Mire
(43°N 7°W)
Mercury accumulation rate (Hg-AR in µg m-2 yr-1)
Calendar Age (year BC /AD)

Fig. 7